JOURNAL OF GUIDANCE, CONTROL, AND DYNAMICS
Vol. 24, No. 1, January–February 2001

Active Control of Flutter in Compressible Flow and Its Aeroelastic Scaling

P. P. Friedmann* and E. Presente†
University of California, Los Angeles, California 90095-1597

A new two-pronged approach suitable for the general aeroelastic and aeroservoelastic scaling of any aeroelastic configuration is presented. The method produces aeroelastic scaling laws for general configurations, and it is particularly useful for situations involving active controls and smart-materials-based actuation. This approach is illustrated by applying it to a two-dimensional wing section in compressible flow, combined with a trailing-edge control surface. Augmented aerodynamic states are reconstructed using a Kalman filter, and linear optimal control is used to design a full-state feedback flutter suppression controller. Constraints on actuator deflection and rate are also considered. In a second example, flutter suppression for a typical cross section with a conventional trailing-edge control surface is compared with that obtained with piezoelectric actuation utilizing bend/twist coupling.

Nomenclature

$[A]$	=	system matrix
$[A_H]$	=	Hamiltonian system matrix
a	=	nondimensional offset between elastic axis (EA) and midchord
$[B]$	=	open-loop control matrix in state space
b	=	airfoil semichord
$[C]$	=	observation matrix, $y(t) = [C]\{x(t)\}$
$C(k)$	=	Theodorsen's lift deficiency function
C_h, C_l, C_m	=	hinge moment, lift, and pitch moment coefficients per unit span
C_P, $\bar{C}_P$	=	power coefficient and its average value
$[C_0]$, $[C_1]$, $[C_2]$ $[D]$, $[E]$, $[R]$	=	constant aerodynamic matrices in state-space formulation
c_β	=	nondimensional flap hinge location
G	=	shear modulus of plate wing section
G_H	=	shear modulus of honeycomb
G_{LT}	=	shear modulus of composite material
H, $\bar{H}$	=	hinge moment per unit span and its nondimensional value
h, h_0	=	plunge displacement at the EA and its initial condition
I_{EA}	=	wing section mass moment of inertia about its EA, per unit span
I_β	=	control surface mass moment of inertia about its hinge, per unit span
J	=	cost function
J_p	=	cross section polar moment of inertia
$[K]$	=	modified wing section nondimensional stiffness matrix
$[\bar{K}]$	=	typical wing section nondimensional stiffness matrix
K_h	=	spring stiffness in plunge
K_α	=	spring stiffness in torsion
K_β	=	control surface torsional stiffness
k	=	reduced frequency, $\omega b/V$
L	=	lift force per unit span
M	=	Mach number
$[M]$	=	modified nondimensional mass matrix
$[\bar{M}]$	=	nondimensional mass matrix
M_{EA}	=	pitch moment per unit span acting at the EA
m	=	wing section mass per unit span
P, $\bar{P}$, $\bar{P}_{\mathrm{av}}$	=	power, its nondimensional and average nondimensional value
$[P]$	=	Riccati matrix
p, $\bar{p}$	=	pressure and its nondimensional value, $p/\frac{1}{2}\rho V^2$
$[Q]$	=	observer Riccati matrix
$\{q\}$	=	displacements vector
r_α	=	wing section radius of gyration about its EA
r_β	=	flap radius of gyration about its hinge
s, $\bar{s}$	=	Laplace variable and its modified value, $\bar{s} = (b/V)s$
$T_1, \ldots, T_{19}$	=	coefficients for Theodorsen's theory
t, $\bar{t}$	=	time and its nondimensional value
t_C	=	composite material ply thickness
t_H	=	honeycomb thickness
$\bar{t}_i$, $\bar{t}_f$, $\bar{t}_1$, $\bar{t}_2$	=	various nondimensional time points
t_t	=	total airfoil thickness
V, $\bar{V}$	=	freestream velocity and its nondimensional value, $V/\omega_\alpha b$
V_D, $\bar{V}_D$	=	divergence velocity and its nondimensional value
V_F, $\bar{V}_F$	=	flutter velocity and its nondimensional value
$[V_1]$, $[V_2]$	=	state excitation noise intensity and measurement noise intensity
$\{x\}$	=	state vector
x_α	=	nondimensional static moment of the airfoil about its EA, for undeflected flap
x_β	=	nondimensional static moment of the flap about its hinge axis
y	=	output measurement
α	=	airfoil angle of attack
β	=	flap deflection angle
ζ	=	damping coefficient
η_a	=	augmented aerodynamic state vector
θ_f	=	flap hinge location
μ	=	mass ratio, $m/\pi\rho b^2$
ξ	=	nondimensional plunge displacement, h/b
ρ	=	air density
ϕ_1, ϕ_2	=	phase lag angles
ω_h	=	natural frequency in plunge, $\sqrt{(K_h/m)}$
ω_α	=	natural frequency in pitch, $\sqrt{(K_\alpha/I_{\mathrm{EA}})}$
ω_β	=	natural frequency of flap, $\sqrt{(K_\beta/I_\beta)}$
$(^*)$	=	nondimensional time derivative, $\mathrm{d}(\,)/\mathrm{d}\bar{t}$

Received 30 July 1999; revision received 1 May 2000; accepted for publication 1 May 2000.

*Professor, Mechanical and Aerospace Engineering Department; currently François-Xavier Bagnoud Professor, Department of Aerospace Engineering, University of Michigan, Ann Arbor, MI 48109-2140. Fellow AIAA.

†Ph.D. Candidate, Mechanical and Aerospace Engineering Department; currently Analyst/Engineer, Advanced Technology Center, Elbit Systems, Haifa, Israel.

Introduction

THE field of aeroservoelasticity has been one of the central subjects in aeroelasticity during the last thirty years. Excellent

surveys on aeroservoelasticity can be found in Refs. 1–3. Early theoretical and experimental studies in aeroservoelasticity were performed in frequency domain. This approach was dictated by the frequency domain unsteady aerodynamic theories, limited to simple harmonic motions, that were in widespread use until the mid-1970s.[4,5] Aeroservoelastic studies performed in frequency domain are inconvenient because they provide limited information on system behavior before and after flutter. Edwards[6] was among the first to recognize the need for time domain aerodynamics in aeroservoelasticity, and by developing the time domain approximation to earlier frequency domain theories, he initiated the use of multi-input/multi-output control laws for flutter suppression. Roger[7] extended Edwards's approach and used it to demonstrate active flutter suppression in a flight test. Since then, numerous studies have been conducted to demonstrate active flutter suppression in flight or in wind-tunnel tests.

Recent advances in the area of smart structures have led to the use of such materials as actuators for aeroservoelastic applications. The attractiveness of such materials is their potential for introducing continuous structural deformations of the lifting surface that can be exploited to manipulate the unsteady aerodynamic loads and prevent undesirable aeroelastic effects such as flutter. Some of the more notable studies in this area include the work of Ehlers and Weisshaar[8] that has analyzed the application of piezoelectric materials to the control of static aeroelastic problems in a composite wing. Heeg et al.[9,10] have conducted several studies demonstrating flutter suppression using piezoelectric actuation on small-scale wind-tunnel models in incompressible flow. Other studies[11] have also looked into static aeroelastic control using piezoelectric actuation. Later this research was extended to flutter suppression using piezoelectric actuation,[12–14] culminating in a wind-tunnel test of a swept wing, controlled by piezoelectric patches. An increase in flutter dynamic pressure of approximately 12% was demonstrated in these tests.[15] Although the potential of piezoelectric actuators in aeroservoelasticity is substantial, currently such materials have major limitations on their stroke and force producing capabilities. Therefore, most of the successful demonstration tests were conducted on small models in incompressible flow. Aeroelastic scaling has been disregarded and the question of how one would scale such actuators for different sized models, or an actual full-scale vehicle, has not been carefully addressed.

During the last forty years aeroelastically scaled wind-tunnel models have been widely used in testing, and aeroelastic scaling laws that enable one to relate wind-tunnel test results to the behavior of the full-scale system have played an important role in aeroelasticity. Such scaling laws have relied on dimensional analysis to establish a set of scaling parameters used for aeroelastically scaled models, suitable for wind-tunnel testing.[16–18] More refined laws can be obtained using similarity solutions, which represent closed-form solutions to the equations of motion. However, for complex aeroelastic problems such solutions are impractical.[19] It is important to emphasize that since the 1960s practically no research has been done on aeroelastic or aeroservoelastic scaling.

The general thrust of this paper is the development of innovative scaling laws for aeroelastic problems in compressible flow, where control is implemented either by conventional trailing-edge surfaces, that is, flaps or by piezoelectric induced actuation, so as to expand the flutter margin. A new two-pronged approach is used, in which basic similarity laws are obtained using typical cross-sectional information and dimensional analysis, resembling the conventional, or classical, approach. In parallel simulations, playing the role of "similarity solutions," are obtained for each of the aeroservoelastic problems for which innovative scaling laws are desired.

To achieve this general objective, several specific goals are pursued, namely, 1) development of a time-domain-based aeroservoelastic simulation capability for a typical cross section in compressible flow, using optimal control theory and a conventional trailing-edge flap/control device; 2) presentation of a new, two-pronged, approach for the development of modern aeroelastic scaling laws and implementation of it for the aeroservoelastic problem being considered; 3) development of scaling laws for aeroservoelastic problems, emphasizing scaling requirements for actuator forces, hinge moments, and power, using the simulation capability developed; and 4) application of the tools developed to several sample problems.

This research shows how results obtained from aeroservoelastic testing, conducted on small aeroelastically scaled wind-tunnel models, can be related to much larger models or the full-scale vehicle. Thus, the paper constitutes an important contribution to the state of the art.

Aeroservoelastic Model

Aeroelastic Model

The aeroelastic model consists of a typical cross section of a wing with plunge and pitch degrees of freedom, combined with a trailing-edge control surface representing an actively controlled flap, as shown in Fig. 1. The equations of motion of the system are obtained from Lagrange's equations. The equations, in nondimensional matrix form, with viscous damping terms are

$$[\bar{M}]\{\ddot{q}\} + [\bar{C}]\{\dot{q}\} + [\bar{K}]\{q\} = (\bar{V}^2/\pi\mu)\{-C_l \quad 2C_m \quad 2C_h\}^T \tag{1}$$

where the nondimensional time $\bar{t} = \omega_\alpha t$ is used. The damping matrix $[\bar{C}]$ is given by

$$[\bar{C}] = 2\begin{bmatrix} (\omega_h/\omega_\alpha)\zeta & 0 & 0 \\ 0 & \zeta & 0 \\ 0 & 0 & (\omega_\beta/\omega_\alpha)\zeta \end{bmatrix} \tag{2}$$

The unsteady aerodynamic loads in Eq. (1) can be obtained by various methods. For incompressible flow, Theodorsen's theory[20] is used, whereas for the compressible case the doublet-lattice method (DLM)[21] is a convenient tool for generating frequency domain oscillatory loads. The general form of the compressible aerodynamic loads acting on a typical section is given in Ref. 16. The pressure distribution over the airfoil is related to the downwash velocity through a kernel function, given by

$$\bar{w}(x) = \frac{1}{8\pi}\int_{-b}^{b} K(x, \eta, k, M)\bar{p}(\eta)\,\mathrm{d}\eta \tag{3}$$

In the DLM, the airfoil is divided into segments and downwash boundary conditions at each segment are imposed. The solution obtained from Eq. (3) yields the distribution of pressure over the airfoil for a given Mach number, reduced frequency, and location of flap hinge combination, for a kernel function $K(x, \eta, k, M)$ given in Ref. 16 (p. 235). Once the pressure distribution over the airfoil is found, aerodynamic loads, lift, pitching moment, and hinge moment are found from an appropriate integration process.

The frequency domain aerodynamic loads are transformed into the time domain using Roger's approximation.[7] The approximation requires first a transformation of the frequency domain loads into the Laplace domain. Subsequently, these loads are expressed as a linear combination of the system states:

$$\{-C_l(\bar{s}) \quad 2C_m(\bar{s}) \quad 2C_h(\bar{s})\}^T = \big([C_0] + [C_1]\bar{s} + [C_2]\bar{s}^2 + [\bar{D}]([I]\bar{s} - [R])^{-1}[E]\bar{s}\big)\{q(\bar{s})\} \tag{4}$$

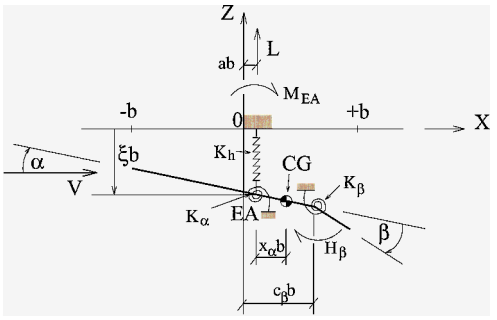

Fig. 1 Definition of parameters for three-degree-of-freedom aeroservoelastic model.

A vector of aerodynamic lag states is introduced by

$$\{\eta_a(\bar{s})\} = ([I]\bar{s} - [R])^{-1}[E]\{q(\bar{s})\}\bar{s} \tag{5}$$

Combining Eqs. (4) and (5) and transforming them to the time domain yields

$$([\bar{M}] - (1/\pi\mu)[C_2])\{\ddot{q}\} + ([\bar{C}] - (\bar{V}/\pi\mu)[C_1])\{\dot{q}\}$$
$$+ \left([\bar{K}] - (\bar{V}^2/\pi\mu)[C_0]\right)\{q\} - (\bar{V}^2/\pi\mu)[\bar{D}]\{\eta_a(\bar{t})\} = 0 \tag{6}$$

Equation (6) is rewritten in first-order state variable form and combining it with Eq. (5) yields the open-loop equation of motion in state space

$$\{\dot{x}\} = [A]\{x(\bar{t})\} \tag{7}$$

where

$$[A] = \begin{bmatrix} 0 & [I] & 0 \\ -[M]^{-1}[K] & -[M]^{-1}[C] & [M]^{-1}[D] \\ 0 & [E] & \bar{V}[R] \end{bmatrix}$$

$$\{x\} = \begin{Bmatrix} \{q\} \\ \{\dot{q}\} \\ \{\eta_a\} \end{Bmatrix}$$

and the matrices used in $[A]$ are

$$[M] = [\bar{M}] - (1/\pi\mu)[C_2], \qquad [C] = [\bar{C}] - (\bar{V}/\pi\mu)[C_1]$$
$$[K] = [\bar{K}] - (\bar{V}^2/\pi\mu)[C_0], \qquad [D] = (\bar{V}^2/\pi\mu)[\bar{D}]$$

Stability of the open-loop system is governed by the eigenvalues of Eq. (7), which are usually represented by root locus plots.

The trailing-edge control surface is used for flutter suppression. The control scheme applies an external hinge moment to the control surface that modifies the aerodynamic loads acting on the typical cross section. The aeroservoelastic equation of motion is similar to Eq. (6):

$$[M]\{\ddot{q}\} + [C]\{\dot{q}\} + [K]\{q(\bar{t})\} - [D]\{\eta_a(\bar{t})\} = H_e\{0 \quad 0 \quad 1\}^T \tag{8}$$

which, in first-order form, is written as

$$\{\dot{x}\} = [A]\{x(\bar{t})\} + [B]\{u(\bar{t})\} \tag{9}$$

where $[A]$ and $\{x\}$ were defined earlier and

$$[B] = \begin{bmatrix} \{0\} \\ [M]^{-1}\{0 \quad 0 \quad 1\}^T \\ \{0\} \end{bmatrix}, \qquad \{u(\bar{t})\} = H_e$$

Control Approach

A somewhat idealized approach to flutter suppression is the use of optimal control theory with full state feedback. In this case, the objective function for flutter suppression is represented by[6,12,22]

$$J = \int_{\bar{t}_i}^{\bar{t}_f} (\{x(\bar{t})\}^T[\bar{Q}]\{x\} + \lambda\{u(\bar{t})\}^T[\bar{R}]\{u\})\,\mathrm{d}\bar{t} \tag{10}$$

where $[\bar{Q}]$ is a nonnegative cost weighting matrix of the states, and $[\bar{R}]$ is a positive-definite weighting matrix involving the control; these are often chosen to be diagonal.[22] The positive weighting constant λ determines the ratio between state and control cost. The solution to the linear optimal control problem is provided by the solution to the Riccati differential equation,[23] which is obtained numerically. The solution to the Riccati differential equation approaches that of the algebraic equation when $\bar{t}_f \to \infty$. It is easier to obtain and frequently used.[22,24] This solution can be obtained from the Hamiltonian matrix of the system, given by[23]

$$[A_H] = \begin{pmatrix} [A] & (1/\lambda)[B][\bar{R}]^{-1}[B]^T \\ -[\bar{Q}] & -[A]^T \end{pmatrix} \tag{11}$$

The eigenvalues of $[A_H]$ are symmetric with respect to both real and imaginary axes. Each eigenvalue with a positive real part has an image eigenvalue with a negative real part. Only the stable eigenvalues are considered. It can be shown that the number of eigenvalues with negative real parts is equal to the number of eigenvalues of the original open-loop system and that the closed-loop system is always stable. The solution to the Riccati algebraic equation is based on Potter's method,[25] and the optimal control law is given by

$$\{u(\bar{t})\}_{\text{opt}} = -(1/\lambda)[\bar{R}]^{-1}[B]^T[P]\{x(\bar{t})\} \tag{12}$$

The closed-loop dynamic equation of motion is[23]

$$\{\dot{x}\} = ([A] - (1/\lambda)[B][\bar{R}]^{-1}[B]^T[P])\{x(\bar{t})\} \tag{13}$$

The control design described does not account for any constraints such as deflection or rate limits on the trailing-edge control surface. Addition of these constraints to the cost function in Eq. (10) does not affect the result of the linear optimal control theory.[26] A potentially rewarding alternative is to recognize that control activity constraints lead to a nonlinear problem and use adaptive control for flutter suppression. The studies described in Refs. 27–29 indicate that adaptive control may be a suitable tool for flutter suppression in the presence of nonlinearities.

The control approach based on full state feedback requires knowledge of the augmented aerodynamic states. The augmented aerodynamic states cannot be measured and have to be reconstructed from the time response. This is accomplished using a Kalman filter. The steady-state observer Riccati matrix $[Q]$ and the steady-state observer gain matrix $[K]$ are found in a similar manner to the calculation of the algebraic Riccati matrix $[P]$ and the closed-loop control law gain matrix.[23] A new Hamiltonian matrix is formed for the algebraic Riccati observer equation:

$$[A_H] = \begin{pmatrix} [A]^T & -[C]^T[V_2]^{-1}[C] \\ -[V_1] & -[A] \end{pmatrix} \tag{14}$$

and a solution to the matrix $[Q]$, similar to that explained earlier for the Riccati matrix $[P]$, leads to the steady-state observer gain matrix[23]

$$[K] = [Q][C]^T[V_2]^{-1} \tag{15}$$

It is important to determine the hinge moment requirements needed for control surface actuation and the power required for flutter suppression. These quantities are required for practical implementations of flutter suppression systems

$$\bar{H} = H|\ mb^2\omega_\alpha^2 = 2(\bar{V}^2/\pi\mu)C_h \tag{16}$$

The instantaneous power is given by

$$P(\bar{t}) = H(\bar{t})\dot{\beta}(\bar{t}) = 2mb^2\omega_\alpha^3(\bar{V}^2/\pi\mu)C_P$$

and in nondimensional form its average value becomes

$$\bar{P}_{\text{av}} = 2\frac{\bar{V}^2}{\pi\mu}\frac{1}{\bar{t}_2 - \bar{t}_1}\int_{\bar{t}_1}^{\bar{t}_2} C_P(\bar{t})\,\mathrm{d}\bar{t} \tag{17}$$

For the cases considered in this study, the average power in Eq. (17) represents the power consumed during a period when the response of the wing section, due to control activity, reduces by a predetermined amount.

Piezoelectrically Twisted Wing/Airfoil

As indicated earlier, one of the goals of this paper is to obtain equivalence relations between a conventional airfoil/trailing-edge flap combination and a continuously deforming wing section that is piezoelectrically actuated. To achieve this objective, consider an idealized section of the wing structural element used for piezoelectric actuation based on bend/twist coupling, shown in Fig. 2. The typical cross section consists of a layer of honeycomb core between two composite face sheets. Two PZT layers are attached to the top and bottom of the composite cover sheets and resemble the actuation

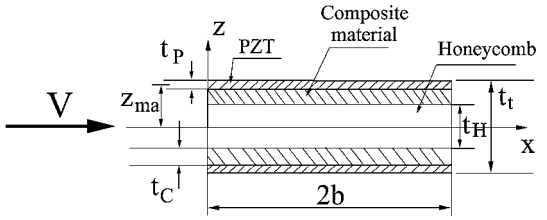

Fig. 2 Idealized wing section using piezoelectric actuation.

patches used in Ref. 12. The change in the pitch moment coefficient, as a result of flap deflections, based on static thin airfoil theory[30] is given by

$$\Delta C_m(t) = \tfrac{1}{2}\sin\theta_f(\cos\theta_f - 1)\beta(t) \tag{18}$$

The static change in pitch moment, due to change in pitch angle, can also be written as

$$\Delta C_m(\bar{t}) = \tfrac{1}{2}\left(a + \tfrac{1}{2}\right)\Delta C_l(\bar{t}) = \pi\left(a + \tfrac{1}{2}\right)\Delta\alpha(\bar{t}) \tag{19}$$

It is assumed that due to the bend/twist coupling, bending moments acting on the section cause only twist along its spanwise axis and that no external twisting moments act on it. Furthermore, it is assumed that the structural element, shown in Fig. 2, represents the cross section of a flat plate type airfoil that is being twisted to produce the same pitching moment that is induced by an actively controlled trailing-edge flap. The power, per unit span, required to twist a flat plate is given by

$$P(\bar{t}) = \omega_\alpha M_y(\bar{t})\frac{\partial^2\alpha}{\partial\bar{t}\,\partial y} \tag{20}$$

where the moment required to twist the plate can be determined, following the analysis described in Ref. 31, for a beamlike wing, from $M_y(\bar{t}) = GJ_p\partial\alpha(\bar{t})/\partial y$. For a constant twist angle along the span, $\partial\alpha/\partial y$ is found directly from the local, instantaneous angle of attack at the typical section. The shear modulus of the typical section, averaged between the various layers but excluding actuation layers, and the polar moment of inertia for a rectangular cross section (Ref. 32, Chapter 5) are given by

$$G = \frac{2G_{\mathrm{LT}}t_C + G_H t_H}{2t_C + t_H}, \qquad J_p = \frac{20}{9}\frac{(t_t/2)^3 b^3}{(t_t/2)^2 + b^2}$$

The equivalent power required to deform the plate section, expressed in terms of an equivalent control flap deflection acting on a typical cross section located at 0.75 semispan, is determined from Eqs. (18–20):

$$P(\bar{t}) = \frac{16}{9}\frac{GJ_p\omega_\alpha}{l^2}\left\{\frac{\sin\theta_f(\cos\theta_f - 1)}{2\pi[a + (1/2)]}\right\}^2\beta(\bar{t})\dot{\beta}(\bar{t}) \tag{21}$$

When Eq. (21) is divided by $m_s b^2\omega_\alpha^3$ and averaged over time, the resulting expression is comparable with Eq. (17). Additional details can be found in Ref. 33.

Aeroelastic and Aeroservoelastic Scaling Laws

Classical Approach to Aeroelastic Scaling

The classical approach to aeroelastic scaling is presented in detail in Ref. 16, Chapter 11. The procedure is best illustrated by considering first the scaling relations in incompressible flow for a two-dimensional airfoil/control surface combination, under the assumption of simple harmonic motion. The extension of these relations to the compressible case is straight forward. For this case one has

$$\begin{Bmatrix}\xi(t)\\ \alpha(t)\\ \beta(t)\end{Bmatrix} = \begin{Bmatrix}\xi_0 e^{i\omega t}\\ \alpha_0\exp(i\omega t + \phi_1)\\ \beta_0\exp(i\omega t + \phi_2)\end{Bmatrix} = \begin{Bmatrix}\xi_0\exp[i(\omega/\omega_\alpha)\bar{t}]\\ \alpha_0\exp[i(\omega/\omega_\alpha)\bar{t} + \phi_1]\\ \beta_0\exp[i(\omega/\omega_\alpha)\bar{t} + \phi_2]\end{Bmatrix} \tag{22}$$

The loads corresponding to Theodorsen's theory[20] are

$$\begin{Bmatrix}-C_l\\ 2C_m\\ 2C_h\end{Bmatrix} = \frac{1}{\bar{V}^2}\begin{bmatrix}-\pi & \pi a & T_1\\ \pi a & -\pi\left(\frac{1}{8} + a^2\right) & -2T_{13}\\ T_1 & -2T_{13} & \frac{1}{\pi}T_3\end{bmatrix}\{\ddot{q}\} + \frac{1}{\bar{V}}\begin{bmatrix}0 & -\pi & -T_4\\ 0 & \pi\left(a - \frac{1}{2}\right) & -T_{16}\\ 0 & -T_{17} & -(1/\pi)T_{19}\end{bmatrix}\{\dot{q}\} + \begin{bmatrix}0 & 0 & 0\\ 0 & 0 & -T_{15}\\ 0 & 0 & -(1/\pi)T_{18}\end{bmatrix}\{q\}$$
$$+ C(k)\left(\begin{bmatrix}0 & -2\pi & -2T_{10}\\ 0 & 2\pi\left(\frac{1}{2} + a\right) & 2\left(\frac{1}{2} + a\right)T_{10}\\ 0 & -T_{12} & -\frac{T_{10}T_{12}}{\pi}\end{bmatrix}\{q\} + \frac{1}{\bar{V}}\begin{bmatrix}-2\pi & -2\pi\left(\frac{1}{2} - a\right) & -T_{11}\\ 2\pi\left(\frac{1}{2} + a\right) & 2\pi\left(\frac{1}{4} - a^2\right) & T_{11}\left(\frac{1}{2} + a\right)\\ -T_{12} & -T_{12}\left(\frac{1}{2} - a\right) & -\frac{T_{11}T_{12}}{2\pi}\end{bmatrix}\{\dot{q}\}\right) \tag{23}$$

Values of T_1–T_{14} are defined in Ref. 20, and T_{15} through T_{19} are convenient combinations of the first $14T_i$ as indicated in Ref. 34. The quantities T_i depend only on the nondimensional hinge location c_β and the nondimensional offset a. When Eqs. (22) and (23) are substituted into Eq. (1), neglecting damping effects and dividing by $(\omega/\omega_\alpha)^2$ yields

$$-\xi_0 - x_\alpha\alpha_0 e^{i\phi_1} - x_\beta\beta_0 e^{i\phi_2} + (\omega_\alpha/\omega)^2(\omega_h/\omega_\alpha)^2\xi_0 = F_1(c_\beta, a, k, \mu, \xi_0, \alpha_0, \phi_1, \beta_0, \phi_2)$$
$$-x_\alpha\xi_0 - r_\alpha^2\alpha_0 e^{i\phi_1} - \left[r_\beta^2 + (c_\beta - a)x_\beta\right]\beta_0 e^{i\phi_2} + r_\alpha^2(\omega_\alpha/\omega)^2\alpha_0 e^{i\phi_1} = F_2(c_\beta, a, k, \mu, \xi_0, \alpha_0, \phi_1, \beta_0, \phi_2)$$
$$-x_\beta\xi_0 - \left[r_\beta^2 + (c_\beta - a)x_\beta\right]\alpha_0 e^{i\phi_1} - r_\beta^2\beta_0 e^{i\phi_2} + r_\beta^2(\omega_\alpha/\omega)^2(\omega_\beta/\omega_\alpha)^2\beta_0 e^{i\phi_2} = F_3(c_\beta, a, k, \mu, \xi_0, \alpha_0, \phi_1, \beta_0, \phi_2) \tag{24}$$

A convenient rule of thumb derived by Buckingham states that the nondimensional solution can then be written in terms of a reduced set of nondimensional combinations that consist of $n - k$ parameters, where n are the original parameters, and $k = 3$ are the primary parameters, mass M, length L, and time T. The nondimensional parameters that can be extracted from Eqs. (24), using Buckingham's π theorem, Ref. 16, p. 698, are listed hereafter:

$$\xi_0 = \frac{h_0}{b}, \qquad k = \frac{\omega b}{V}, \qquad \mu = \frac{m}{\pi\rho b^2}, \qquad \frac{\omega_h}{\omega_\alpha} = \sqrt{\frac{K_h/m}{K_\alpha/I_{\mathrm{EA}}}}$$
$$\frac{\omega_\beta}{\omega_\alpha}, \qquad \frac{\omega_\alpha}{\omega}, \qquad r_\alpha^2, \qquad r_\beta^2, \qquad c_\beta, \qquad a, \qquad x_\alpha = \frac{S_\alpha}{mb}$$
$$x_\beta = \frac{S_\beta}{mb}, \qquad \alpha_0, \qquad \beta_0, \qquad \phi_1, \qquad \phi_2$$

The first 12 parameters can be expressed as combinations of the three primary variables, whereas the last 4 are nondimensional quantities. For aeroelastic stability, the quantities of interest are $\omega_F b/V_F$, ω_F/ω_α, and $h_0/b\alpha_0$, where the subscript F refers to the flutter condition. For aeroelastic similarity all other nondimensional parameters such as μ, (ω_h/ω_α), $(\omega_\beta/\omega_\alpha)$, ..., etc., for the model, must have the appropriate values. The external shape, that is, airfoil type, and Reynolds number also have to be retained. When compressible flow is considered the list of sixteen parameters given has to be augmented by an additional parameter M.

Flutter conditions of similar structural configurations imply that their nondimensional flutter velocity is kept constant, as well as the Mach number. The pitch frequency of a scaled model relates to that of the full-scale configuration according to the geometrical scaling ratio

$$(\omega_\alpha)_m/(\omega_\alpha)_w = b_w/b_m \tag{25}$$

where subscript m stands for model and subscript w for the prototype.

The scaling of damping properties also needs to be addressed. Equations (1) and (2) imply that the damping of each mode is related to the natural frequency associated with that mode. Once the natural frequencies change, the damping coefficient of a corresponding mode needs to be modified to match the appropriate damping loads:

$$\zeta_m/\zeta_w = (\omega_\alpha)_w/(\omega_\alpha)_m = b_m/b_w \tag{26}$$

The aeroelastic scaling considerations discussed are based on classical solutions that are obtained from Eqs. (1) and (22–24).

Refined Aeroelastic Scaling Procedure

For modern applications, the classical approach is inadequate for several reasons. The control system may experience saturation, free play, and friction, which introduce nonlinear effects that cannot be represented by the simple linear equations that have been used in deriving aeroelastic scaling relations. Furthermore, the aerodynamic loads may be obtained from computational fluid dynamic codes involving the solutions of the Euler or Navier–Stokes equations. For such cases the aeroelastic model will contain aerodynamic nonlinearities.[28] In such situations the aeroelastic or aeroservoelastic studies are based on refined computer simulations. To accomodate these more complicated configurations, an alternative, refined approach to aeroelastic scaling was developed. It is based on a combination of the classical approach and a computer simulation of the specific problem being considered.

Figure 3 depicts the new two-pronged approach that was developed for generating refined scaling laws that are applicable to any general linear or nonlinear aeroelastic or aeroservoelastic problem. In this approach, basic scaling requirements are established using typical cross-sectional information and dimensional analysis, in a manner that resembles the conventional, or classical, procedure. This process is represented by the left-hand branch in Fig. 3. In parallel, solutions based on computer simulations are obtained for each aeroelastic or aeroservoelastic problem for which refined scaling laws are required. These computer simulations represent numerical similarity solutions that can replace the analytical, closed-form similarity solutions that are usually sought in the framework of mathematical similarity theory.[19] This portion of the procedure is represented by the right-hand branch of Fig. 3. By combining the requirements based on the classical approach with those based on the computer simulation, a set of expanded or refined aeroelastic scaling requirements is obtained.

These computer simulations enable one to account for additional effects, such as presence of multiple control surfaces and stores, shock wave motion in transonic flow, saturation, free play, and separation. This approach easily accounts for the presence of the control system, a fundamental need in aeroelasticity. For such applications the nondimensional frequency variable ω_α/ω is replaced by a nondimensional time variable $\bar{t} = \omega_\alpha t$, and the reduced frequency is replaced by the nondimensional velocity $\bar{V} = V/\omega_\alpha b$. Computer simulations are particularly suitable for examining the intricate scaling requirements governing control power, control forces, and hinge moments, which play an important role when extrapolating the model tests to the full-scale configuration.

Finally, note that this approach is particularly suitable for applications that involve the use of adaptive materials based actuation for the modification and control of aeroelastic problems. The two-pronged approach can easily account for all of the intricate details associated with this class of materials.

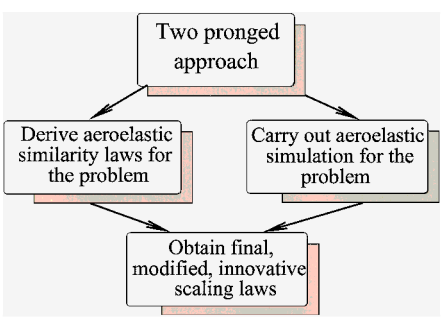

Fig. 3 Two-pronged approach for generating refined aeroelastic scaling laws.

Results and Discussion

Open- and Closed-Loop Results for Baseline Configuration

Results presented were calculated for a typical cross section in subsonic flow using a computer code implementing the time domain aeroservoelastic analysis described earlier in this paper. Airfoil parameters used to generate the results were selected to resemble values for an executive jet type of aircraft with a wing span of 52.6 ft, semichord length of $b = 35.0$ in. and a pitch frequency of $\omega_\alpha = 110.0$ rad/s: $a = -0.2$, $c_\beta = 0.8$, $x_\alpha = 0.2$, $x_\beta = -0.008$, $r_\alpha^2 = 0.25$, $r_\beta^2 = 0.036$, $\omega_h/\omega_\alpha = 0.25$, $\omega_\beta/\omega_\alpha = 2.0$, and a structural damping coefficient of $\zeta = 0.002$. Estimations for a wing weight, from which the mass ratio was deduced, were found in Refs. 35 and 36. A value of $\mu = 25.6$ was chosen to represent the typical cross section at sea-level conditions.

Aerodynamic loads were calculated from a DLM code, for a specific Mach number, and approximated in the time domain using Roger's approximation.[7] A reduced frequency range of $0.000 \le k \le 1.300$ was used for the analyses. Results shown were calculated with four aerodynamic lag roots located at $\gamma_1 = 0.0250$, $\gamma_2 = 0.1500$, $\gamma_3 = 0.6000$, and $\gamma_4 = 1.2000$.

Stability analysis for a typical cross section representative of this full-scale configuration yields a matched point flutter Mach number of $M = 0.702$. Figure 4 depicts the open-loop root locus plots for this configuration. The nondimensional open-loop flutter velocity found was $\bar{V}_F = 2.441$, which at standard sea-level conditions corresponds to a true velocity of $V = 783.2$ ft/s or a flight Mach number of $M = 0.702$.

The closed-loop results were generated for a diagonal state cost matrix in which all of the states had a unit cost, that is, $\bar{Q}_{ii} = 1.00$. The $\bar{R}$ matrix was reduced to a single scalar component given by $\bar{R} = 1.00$, and the cost function parameter was set to $\lambda = 100.00$. The root locus plots in Fig. 5 illustrate the behavior of the closed-loop configuration. Three modes are shown. The unstable part of the open-loop root locus, shown in Fig. 4, is reflected to the stable half of the s plane in Fig. 5. A precise reflection occurs only when the control cost parameter is very high.[6,23]

When examining the time domain system behavior two initial conditions were used. A ramp input of 10 deg/s angle-of-attack rate was applied to the system as an initial disturbance. This is denoted as case I in the discussion that follows. Control surface saturation limits

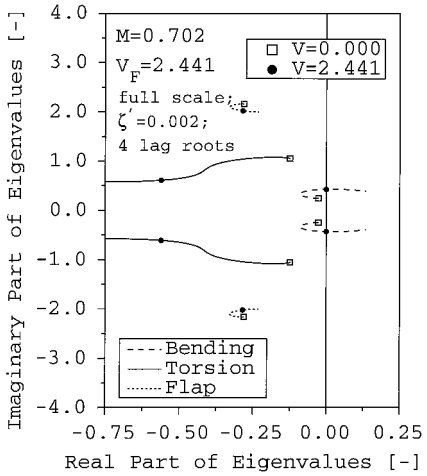

Fig. 4 Open-loop root locus of full-scale configuration at $M = 0.702$.

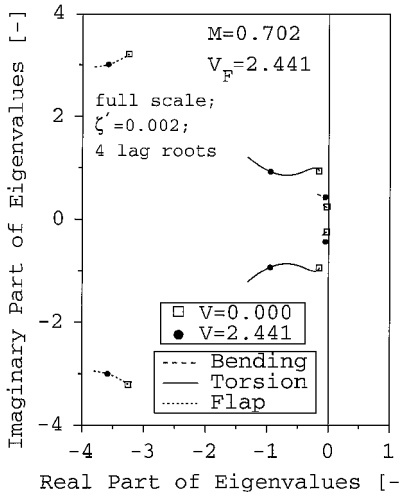

Fig. 5 Closed-loop root locus of full-scale configuration at $M = 0.702$.

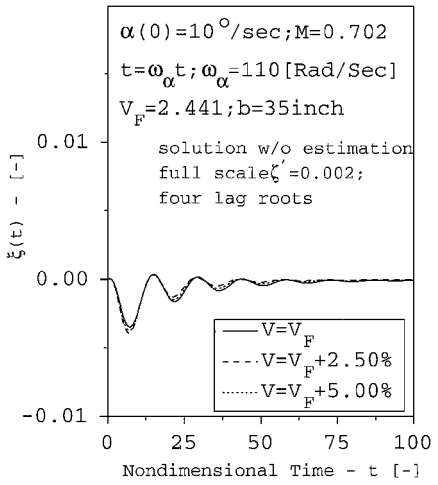

Fig. 6 Closed-loop time history of plunge displacement for the full-scale configuration at $M = 0.702$.

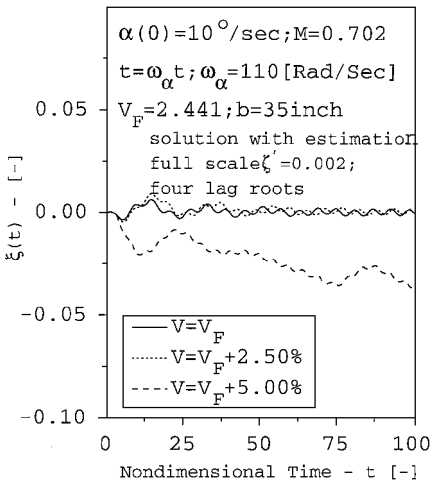

Fig. 7 Closed-loop time history of full-scale configuration in plunge $\xi(\bar{t})$, case I.

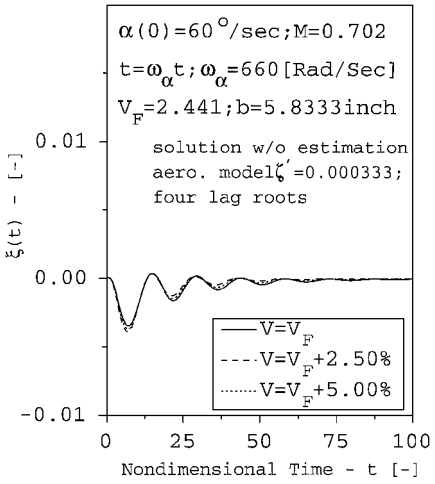

Fig. 8 Closed-loop time history of plunge displacement for the aeroelastically scaled model at $M = 0.702$.

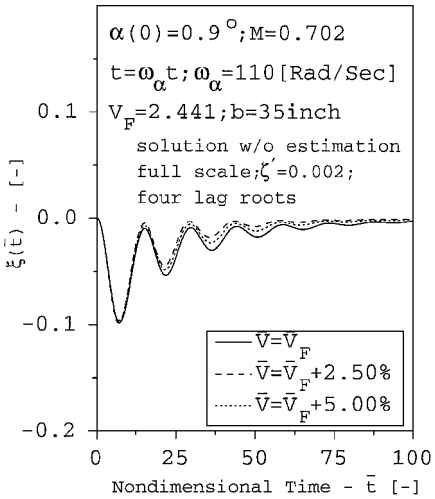

Fig. 9 Closed-loop time history of full-scale configuration plunge displacement $\xi(\bar{t})$, case II.

were selected with typical values of $|\beta_{\max}| \leq 4$ deg, $|\dot{\beta}_{\max}| \leq 90$ deg/s, and a maximum hinge moment of $(H_e)_{\max} = 50{,}000$ lb-in. was used for a flap span of 68.5 in. These values yield a typical cross section hinge moment saturation value of 729.3 lb-in./in. A second case with initial conditions consisting of a 0.9-deg step function in angle of attack, denoted case II, was also considered. It corresponds, at $M = 0.702$, to a gust of approximately 12.5 ft/s. Flap control saturation levels similar to case I were used in this case.

Figure 6 depicts a plunge displacement time history plot, for case I, of the full-scale configuration in closed loop at three velocities: $\bar{V}_F$, $1.025\bar{V}_F$, and $1.05\bar{V}_F$. As velocity increases, peak response in plunge also increases; however, values are below 0.05 of a semichord length.

Note that the matched point flutter Mach number of $M = 0.702$ is violated slightly when dealing with velocities that are 2.5 and 5% above the flutter velocity $\bar{V}_F$. This comment is applicable to Figs. 6–12.

To construct a control law it was assumed that all of the augmented aerodynamic states, as well as the structural states, were known. In Figs. 5 and 6 it is shown that the closed-loop system is stable, that after a few oscillations the initial disturbance is dissipated, and that the system returns to its initial undisturbed state under the action of a control law. To estimate the augmented aerodynamic states, state excitation noise and measurement excitation noise intensities were selected. The dynamic system is assumed to be perfectly modeled, and, therefore, state excitation noise intensity was selected as $[V_1] = 0$, and a unit matrix was used for the measurement excitation noise intensity. Figure 7 depicts the plunge motion results for case I, in which four aerodynamic lag roots were used to approximate the aerodynamic states. It appears that at $\bar{V} = \bar{V}_F + 5\%$ results diverge, whereas for cases with slower speeds above flutter the system oscillates without converging. Clearly, reconstruction of the augmented states causes problems. To avoid these problems it was assumed, for the rest of the results generated here, that the augmented aerodynamic states are known exactly and do not need to be reconstructed. Note, however, that for practical situations the augmented aerodynamic states are not observable and their reconstruction is essential.

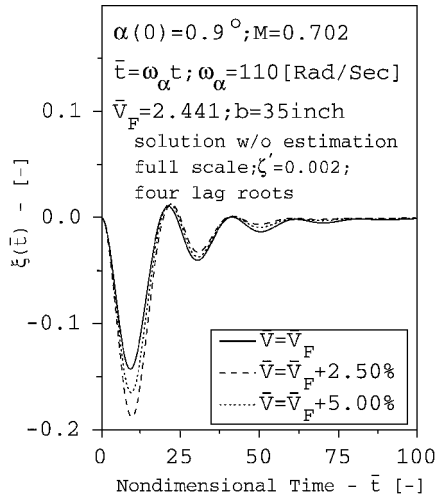

Fig. 10 Closed-loop time history of full-scale configuration in plunge $\xi(\bar{t})$, case I, with a different control saturation level.

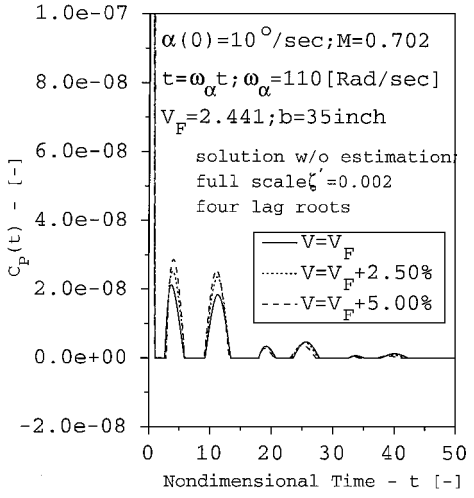

Fig. 11 Closed-loop time history of power coefficient for the full-scale configuration at $M = 0.702$.

Furthermore, the inconveniences associated with this reconstruction have to be addressed.

Aeroelastic Scaling Example

To illustrate the importance of aeroelastic scaling, two approaches to scaling the baseline configuration are explored. For the first case, only geometrical scaling (GSM) of wing dimensions was used. In the second case, aeroelastic scaling (ASM), which requires a change of wing stiffness was implemented. Both cases were assumed to represent 1:6 scaled versions of the full-scale configuration. The ratio between the torsional frequency of the model and that of the full-scale configuration, as indicated by Eq. (25), is related to the GSM between both systems. The ASM pitch frequency was increased by a factor of six. The mass ratio of the ASM also changes. The full-scale configuration flutters at $M = 0.702$, which corresponds to a density ratio of $\rho_0/\rho = 1.2649$. The mass ratio of the ASM was decreased by the same factor to compensate for the drop in fluid density. This ratio for the ASM was $\mu = 20.241$, whereas for the GSM the mass ratio of the baseline configuration was retained. The damping of ASM was also modified according to the relation given in Eq. (26). Table 1 summarizes the parameters describing the two models.

Open-loop results for the baseline and the two scaled configurations are shown in Table 2, depicting flutter velocity, dimensional and nondimensional, Mach number at flutter, flutter frequency, and nondimensional divergence velocity. It is evident that only the ASM has an open-loop behavior similar to the full-scale configuration. The geometrically scaled model becomes unstable at conditions different from those of the full-scale configuration.

Table 1 Comparison of scaling parameters between three typical cross section models

Parameter	Full scale	GSM	ASM
b, in.	35	5.8333	5.8333
ω_α, rad/s	110.0	110.0	660.0
μ	25.6	25.6	20.241
ζ	0.002000	0.002000	0.000333

Table 2 Comparison of stability results between three typical cross section models

Parameter	Full scale	GSM	ASM
$\bar{V}_F$	2.441	2.579	2.441
V_F, ft/s	783.2	137.9	783.2
ω_F, Hz	46.89	55.84	46.89
M_F	0.702	0.123	0.702
$\bar{V}_D$	2.636	3.244	2.636

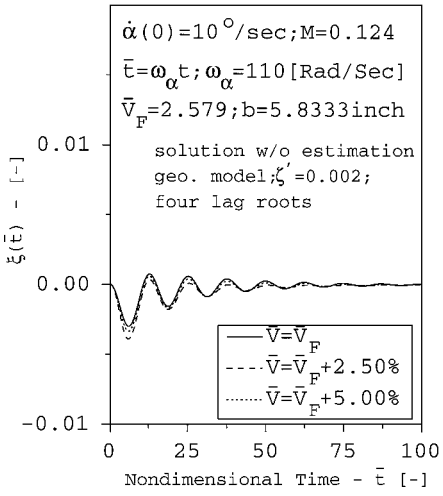

Fig. 12 Closed-loop time history of plunge displacement for the geometrically scaled model at $M = 0.123$.

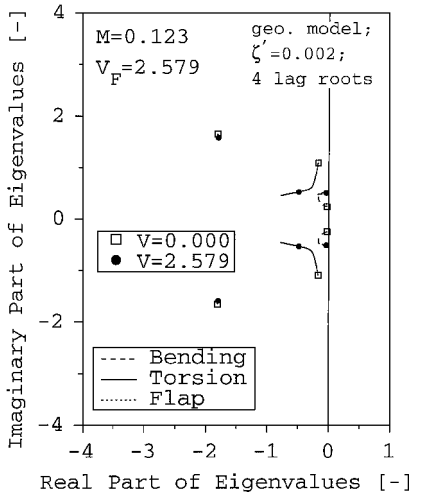

Fig. 13 Closed-loop root locus of geometrically scaled model at $M = 0.123$.

Figures 8 and 9 exhibit the closed-loop root loci of the geometrically and aeroelastically scaled models, respectively. It is evident that the GSM does not display a behavior resembling the full-scale configuration, while the ASM does.

A corresponding time history plot for the GSM is shown in Fig. 10, which depicts plunge displacement. Plunge response of the GSM to the same initial conditions that were applied to the full-scale configuration is very similar to that of the full-scale configuration,

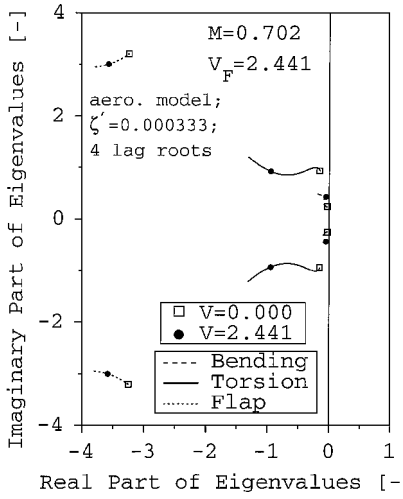

Fig. 14 Closed-loop root locus of aeroelastically scaled model at $M = 0.702$.

and oscillation amplitudes are of the same order of magnitude. Note that close to flutter boundary the systems exhibit similar behavior in the time domain, although they are not similar and will generally behave differently at velocities that exceed the flutter boundary by a considerable amount.

The initial disturbance was nondimensionalized and found to be $\overset{*}{\alpha}(0) = \overset{*}{\alpha}(0)/\omega_\alpha = 0.00158666$. For the ASM case this initial disturbance was applied to the model, and a dimensional value of the similar case was determined as $\dot{\alpha}(0) = \omega_\alpha \overset{*}{\alpha}(0) = 60$ deg/s. The appropriate flap rate limit was also determined from scaling considerations and found to be $|\dot{\beta}_{\max}| \leq 360$ deg/s. In addition, a scaled hinge moment limit was determined, based on the relations in Eq. 16. The hinge moment limit of the ASM was reduced by a scaling factor of $1{:}l^2$ and found to be 20.26[lb-in./in.]. Figure 11 depicts corresponding plunge results for the ASM. Plunge displacement is similar to the corresponding result of the full-scale configuration, shown in Fig. 6.

Influence of Control Saturation

System behavior for case II type of initial conditions was also considered to illustrate saturation and stabilization loss due to nonlinearities associated with stabilization. Time histories for plunge motion, with a control cost parameter of $\lambda = 10^2$, are shown in Fig. 13 for the full-scale configuration, or baseline configuration. Deflection limits were modified to $|\beta_{\max}| \leq 1.5$ deg and their effect on flutter suppression of the baseline configuration studied. Figure 14 exhibits the plunge displacement of the typical section, similar to that depicted in Fig. 13 for the baseline configuration. A plunge of about 15% of the semichord is evident, at flutter conditions, whereas in Fig. 13 a plunge of only 10% is observed. Because of tighter control flap deflection limits, the typical cross section reaches nonlinear regions earlier, and flutter boundaries can be expanded by smaller amounts. For higher velocities above the flutter boundary the control system fails to stabilize the system.[33]

Comparison of Piezoelectric Actuation to a Conventional Trailing-Edge Device

Hinge moments needed for actuation and power required for flutter suppression are important aspects of aeroservoelastic behavior. Two separate cases are examined. The first case considers the hinge moments and power requirements for the baseline, or full-scale, configuration. The second case compares the relative merits of piezoelectric actuation with that of a conventional, equivalent, trailing-edge control surface. Two models were studied. The first was an articulated wing section/trailing-edge control flap combination, with the same properties as the full-scale configuration studied earlier.

Figure 12 depicts time history of the power coefficient required for the full-scale configuration for case I. Negative values of power imply that the system produces power and such contributions were neglected. Because power decreases rapidly, only the first 50 s of nondimensional time history is shown. The average power required

Table 3 Average power required to suppress flutter of a baseline wing section at several nondimensional velocities

$\bar{V}$	$\Delta\bar{V}$, %	$\bar{t}_1$	$\bar{t}_2$	$\bar{C}_P$	P_{av}, hp/s
2.441	0.00	1.700	26.65	$4.254E^{-9}$	$2.1102E^{-5}$
2.502	2.50	1.650	27.150	5.050×10^{-9}	2.6319×10^{-5}
2.563	5.00	1.600	27.550	5.189×10^{-9}	2.8378×10^{-5}

Table 4 Average power required to suppress flutter of a piezoelectrically actuated wing section at several nondimensional velocities

$\bar{V}$	$\bar{t}_1$	$\bar{t}_2$	$\bar{C}_P$	P_{av}, hp/s
2.441	1.700	26.65	2.255×10^{-8}	1.1186×10^{-4}
2.502	1.650	27.150	1.655×10^{-8}	8.6253×10^{-5}
2.563	1.600	27.550	1.436×10^{-8}	7.6222×10^{-5}

to reduce the wing section pitch oscillations by 90% from its maximum value together with the time frame required for this reduction are shown in Table 3. This is a better measure of system performance than instantaneous power. It is evident from Table 3 that only small amounts of power are required for flutter suppression when flying at modest speeds above the open-loop flutter velocity.

The second model, a flat plate employing a continuous twist of the wing section for flutter suppression, had similar properties to those of the plate used in Ref. 12 and shown in Fig. 2. A half-wing-span configuration with a semispan of 26.33 ft and a semichord of 35 in. was used. The plate configuration modeled included an aluminum-based honeycomb and a layer of six glass/epoxy laminates having a $[30^\circ, 30^\circ, 0^\circ]_s$ construction. Other parameters required for modeling this configuration were $(E_L)_a = 8.70$ [Mpsi], $t_P = 0.11667$ in., $Z_{\text{ma}} = 0.70117$ in., $G_{\text{LT}} = 0.87$ [Mpsi], $t_C = 6 \times 0.030$ in., $\nu_C = 0.28$, $G_H = 0.11$ [Mpsi], $t_H = 1.0325$ in., $\nu_H = 0.3$, $d_{31} = 7.09 \times 10^{-9}$ [in./V].

Comparison of the power requirements for flutter suppression for a piezoelectrically twisted wing section and a conventional wing section/flap combination were obtained from the relations described earlier in Eq. (21) and are presented in Table 4. These results are similar to those presented in Table 3 for the baseline configuration.

Limits reported in Ref. 37 are 200 $\mu\varepsilon$ for actuation strains and 200 V for voltage source. The results obained indicate that strains fall within this limit and it appears that PZT materials are suitable candidate materials for flutter suppression. Note that the power requirements of the actively controlled flap are considerably lower than those required for the piezoelectrically twisted wing section. The main reason for this is that piezoelectric actuation requires actual structural deformations of the wing. This additional energy is not needed for the case of the conventional airfoil/flap combination. Additional results can be found in Ref. 33. Note that whereas the power requirements for the piezoelectrically actuated wing take into account all of the effects required to generate wing twist, the same is not true for the flap because the power loss involved in the mechanism associated with flap motion is not accounted for. This additional power may partially offset the difference in power requirement between these two methods of actuation.

Conclusions

This study reexamines the issue of aeroelastic and aeroservoelastic scaling within the framework of modern aeroelasticity. This is a very important and somewhat neglected aspect of aeroelasticity. The principal findings of this study are summarized here:

1) A new, two-pronged approach to aeroelastic and aeroservoelastic scaling was developed. It combines the classical approach with computer simulation of the specific problem. It is capable of providing useful scaling information on hinge moments and power requirements for flutter suppression. It is completely general in scope and applicable to any aeroelastic system.

2) Solutions to the nondimensional aeroelastic or aeroservoelastic problems provide similarity solutions. Only such solutions correctly predict the behavior of a full-scale configuration, as well as that of aeroelastically scaled models. A partially scaled model, such as the

GSM, does not provide accurate predictions of the behavior of a full-scale configuration.

3) Saturation of flap deflection and rate pose realistic limitations on the extent of flutter margin expansion. Saturation introduces a strong nonlinearity that is not addressed by current techniques available in the field of control systems.

4) Power requirements for flutter suppression were calculated for two models of a typical cross section: one with an actively controlled flap and the other with a piezoelectrically actuated continuously distributed twist. The average power required for piezoelectric actuation is significantly larger than that required by a typical wing section employing an actively controlled flap.

5) Using time domain unsteady aerodynamics with full state feedback requires reconstruction of the unsteady aerodynamic states that cannot be observed. This introduces considerable complexity in the aeroservoelastic problem. This issue has been overlooked in previous studies. The reconstruction of such nonobservable states is essential in practical applications.

Acknowledgment

This research grant was supported by the Air Force Office of Scientific Research under Grant F49620-94-1-0400, with Brian Sanders as grant monitor.

References

[1]Noll, T. E., "Aeroservoelasticity," *Flight-Vehicle Materials, Structures, and Dynamics—Assessment and Future Direction*, edited by A. K. Noor and S. L. Venneri, Vol. 5, American Society of Mechanical Engineers, Fairfield, NJ, 1993, Chap. 3, pp. 179–212.

[2]Livne, E., "Integrated Aeroservoelastic Optimization: Status and Direction," *Journal of Aircraft*, Vol. 36, No. 1, 1999, pp. 122–145.

[3]Friedmann, P. P., "Renaissance of Aeroelasticity and Its Future," *Journal of Aircraft*, Vol. 36, No. 1, 1999, pp. 105–121.

[4]Newsom, J. R., Pototzky, A. S., and Abel, I., "Design of a Flutter Suppression System for an Experimental Drone Aircraft," *Journal of Aircraft*, Vol. 22, No. 5, 1985, pp. 380–386.

[5]Roger, K. L., Hodges, G. E., and Felt, L., "Active Flutter Suppression, A Flight Test Demonstration," *Journal of Aircraft*, Vol. 6, No. 12, 1975, pp. 551–556.

[6]Edwards, J. W., "Unsteady Aerodynamic Modeling and Active Aeroelastic Control," Ph.D. Dissertation, Dept. of Aeronautics and Astronautics, Stanford Univ., Stanford, CA, Feb. 1977.

[7]Roger, K. L., "Airplane Math Modeling Methods for Active Control Design," *Structural Aspects of Active Controls*, CP-228, AGARD, Aug. 1977, pp. 4-1–4-11.

[8]Ehlers, S. M., and Weisshaar, T. A., "Static Aeroelastic Behavior of an Adaptive Laminated Piezoelectric Composite Wing," *Proceedings of the 31st AIAA/ASME/ASCE/AHS/ASC Structures, Structural Dynamics, and Materials Conference*, AIAA, Washington, DC, 1990, pp. 1611–1623.

[9]Heeg, J., Scott, R. C., and McGowan, A.-M. R., "Aeroelastic Research Using Smart Structures Concepts," *Aeroelasticity and Fluid Structure Interaction Problems*, edited by P. P. Friedmann and J. C. I. Chang, AD-Vol. 44, American Society of Mechanical Engineers, Chicago, 1994, pp. 161–173.

[10]Heeg, J., McGowan, A., Crawley, E., and Lin, C., "The Piezoelectric Aeroelastic Response Tailoring Investigation," *International Forum on Aeroelasticity and Structural Dynamics 1995*, Royal Aeronautical Society, Manchester, England, U.K., 1995, pp. 8.1–8.11.

[11]Lazarus, K. B., Crawley, E. F., and Bohlmann, J. D., "Static Aeroelastic Control Using Strain Actuated Adaptive Structures," *Journal of Intelligent Material Systems and Structures*, Vol. 2, No. 3, 1991, pp. 386–410.

[12]Lin, C. Y., "Towards Optimal Strain Actuated Aeroelastic Control," Ph.D. Dissertation, Dept. of Aeronautics and Astronautics, Massachusetts Inst. of Technology, Cambridge, MA, Jan. 1996.

[13]Lin, C. Y., Crawley, E. F., and Heeg, J., "Open- and Closed-Loop Results of a Strain-Actuated Active Aeroelastic Wing," *Journal of Aircraft*, Vol. 33, No. 5, 1996, pp. 987–994.

[14]Lazarus, K. B., Crawley, E. F., and Lin, C. Y., "Multivariable Active Lifting Surface Control Using Strain Actuation: Analytical and Experimental Results," *Journal of Aircraft*, Vol. 34, No. 3, 1997, pp. 313–321.

[15]McGowan, A., Heeg, J., and Lake, R. C., "Results of Wind-Tunnel Testing from the Piezoelectric Aeroelastic Response Tailoring Investigation," *Proceedings of the 37th AIAA/ASME/ASCE/AHS/ASC Structures, Structural Dynamics and Materials Conference*, AIAA, Reston, VA, 1996, pp. 1722–1732.

[16]Bisplinghoff, R. L., Ashley, H., and Halfman, R. L., *Aeroelasticity*, Addison–Wesley, Cambridge, MA, 1955.

[17]Hunt, G. K., "Similarity Requirements for Aeroelastic Models of Helicopter Rotors," Aeronautical Research Council, CP 1245, Jan. 1973.

[18]Regier, A. A., "The Use of Scaled Dynamic Models in Several Aerospace Vehicle Studies," *Proceedings of ASME Colloquium on the Use of Models and Scaling in Simulation of Shock and Vibration*, American Society of Mechanical Engineers, New York, 1963, pp. 34–50.

[19]Baker, W. E., Westine, P. S., and Dodge, F. T., *Similarity Methods in Engineering Dynamics: Theory and Practice of Scale Modeling*, rev. ed., Elsevier, New York, 1991.

[20]Theodorsen, T., "General Theory of Aerodynamic Instability and the Mechanism of Flutter," NACA TR 496, 1935.

[21]Albano, E., and Rodden, W. P., "Doublet–Lattice Method for Calculating Lift Distribution on Oscillating Surfaces in Subsonic Flows," *AIAA Journal*, Vol. 7, No. 2, 1969, pp. 279–282.

[22]Mukhopadhyay, V., "Flutter Suppression Control Law Design and Testing for the Active Flexible Wing," *Journal of Aircraft*, Vol. 32, No. 1, 1995, pp. 45–51.

[23]Kwakernaak, H., and Sivan, R., *Linear Optimal Control Systems*, Wiley, New York, 1972.

[24]Dowell, E. H., *A Modern Course in Aeroelasticity*, 3rd ed., Kluwer Academic, Norwell, MA, 1995, Chap. 12.

[25]Potter, J. E., "Matrix Quadratic Solutions," *SIAM Journals on Applied Mathematics*, Vol. 14, No. 3, 1966, pp. 496–501.

[26]Bryson, A. E., Jr., and Ho, Y. C., *Applied Optimal Control*, Hemisphere, Washington, DC, 1975.

[27]Roy, I. D., and Eversman, W., "Adaptive Flutter Suppression of an Unswept Wing," *Journal of Aircraft*, Vol. 33, No. 4, 1996, pp. 775–783.

[28]Friedmann, P. P., Guillot, D., and Presente, E. H., "Adaptive Control of Aeroelastic Instabilities in Transonic Flow and Its Scaling," *Journal of Guidance, Control, and Dynamics*, Vol. 20, No. 6, 1997, pp. 1190–1199.

[29]Eversman, W., and Roy, I. D., "Active Flutter Suppression Using Multi-Input/Multi-Output Adaptive Least Mean Square Control," *Journal of Aircraft*, Vol. 34, No. 2, 1997, pp. 244–250.

[30]Kuethe, A. M., and Chow, C., *Foundations of Aerodynamics*, 4th ed. Wiley, New York, 1986.

[31]Lazarus, K. B., "Multivariable High-Authority Control of Plate-Like Active Lifting Surfaces," Ph.D. Dissertation, Dept. of Aeronautics and Astronautics, Massachusetts Inst. of Technology, Cambridge, MA, June 1992.

[32]Shames, I. H., and Dym, C. L., *Energy and Finite Element Methods in Structural Mechanics*, Taylor and Francis, Washington, DC, 1985.

[33]Presente, E., "Innovative Scaling Laws for Aeroelastic and Aeroservoelastic Problems in Compressible Flow," Ph.D. Dissertation, Mechanical and Aerospace Engineering Dept., Univ. of California, Los Angeles, 1999.

[34]Theodorsen, T., and Garrick, I. E., "Nonstationary Flow About a Wing-Aileron-Tab Combination Including Aerodynamic Balance," NACA TR 736, May, 1942,

[35]Raymer, D. P., *Aircraft Design: A Conceptual Approach*, 2nd ed., AIAA Education Series, AIAA, Washington, DC, 1992.

[36]Nicolai, L. M., *Fundamentals of Aircraft Design*, METS, Inc., San Jose, CA, 1984.

[37]Reich, G. W., van Schoor, M. C., Lin, C. Y., and Crawley, E. F., "An Active Aeroelastic Wing Model for Vibration and Flutter Suppression," *Proceedings of the 36th AIAA/ASME/AHS/ASC Structures, Structural Dynamics, and Materials Conference*, AIAA, Washington, DC, 1995, pp. 314–324.